



OPEN ACCESS

EDITED BY

Claudio Chiastra,
Polytechnic University of Turin, Italy

REVIEWED BY

Monika Colombo,
Aarhus University, Denmark
Quentin Landolff,
Clinique saint hilaire, France

*CORRESPONDENCE

Eric K. W. Poon

✉ epoon@unimelb.edu.au

Patrick W. Serruys

✉ patrick.serruys@universityofgalway.ie

†These authors have contributed equally to this work and share first authorship

RECEIVED 12 November 2025

REVISED 07 January 2026

ACCEPTED 09 January 2026

PUBLISHED 06 February 2026

CITATION

Hatzikostas L, Miyashita K, de Vries R, Sanders B, von Basum G, van Noort K, Dijkstra J, Bourantas CV, Tsai T-Y, Onuma Y, Barlis P, Serruys PW and Poon EKW (2026) Preclinical serial shear stress analysis of a novel strut-free fibrillated bioresorbable polymeric endoluminal graft. *Front. Cardiovasc. Med.* 13:1744904. doi: 10.3389/fcvm.2026.1744904

COPYRIGHT

© 2026 Hatzikostas, Miyashita, de Vries, Sanders, von Basum, van Noort, Dijkstra, Bourantas, Tsai, Onuma, Barlis, Serruys and Poon. This is an open-access article distributed under the terms of the [Creative Commons Attribution License \(CC BY\)](#). The use, distribution or reproduction in other forums is permitted, provided the original author(s) and the copyright owner(s) are credited and that the original publication in this journal is cited, in accordance with accepted academic practice. No use, distribution or reproduction is permitted which does not comply with these terms.

Preclinical serial shear stress analysis of a novel strut-free fibrillated bioresorbable polymeric endoluminal graft

Lucas Hatzikostas^{1,2†}, Kotaro Miyashita^{3†}, Rick de Vries⁴, Bart Sanders⁴, Golo von Basum⁴, Kim van Noort⁴, Jouke Dijkstra⁵, Christos V. Bourantas^{6,7}, Tsung-Ying Tsai³, Yoshinobu Onuma³, Peter Barlis¹, Patrick W. Serruys^{3,8*} and Eric K. W. Poon^{1*}

¹Department of Medicine, Melbourne Medical School, Faculty of Medicine, Dentistry and Health Sciences, The University of Melbourne, Fitzroy, VIC, Australia, ²Department of Cardiology, Royal Melbourne Hospital, Parkville, VIC, Australia, ³Department of Cardiology, University of Galway, Galway, Ireland, ⁴STENTIT B.V., Eindhoven, Netherlands, ⁵Department of Radiology, Leiden University Medical Center, Leiden, Netherlands, ⁶Device and Innovation Centre, William Harvey Research Institute, Queen Mary University of London, London, United Kingdom, ⁷Department of Cardiology, Barts Heart Centre, Barts Health NHS Trust, London, United Kingdom, ⁸Department of Mechanical Engineering, Faculty of Engineering and Information Technology, The University of Melbourne, Melbourne, VIC, Australia

Aim: To characterise near-wall haemodynamics immediately after implantation of a next-generation, strut-free biorestorative endoluminal graft, evaluate changes over 3 months during resorption, and assess whether early flow patterns may influence subsequent remodelling in two preclinical models.

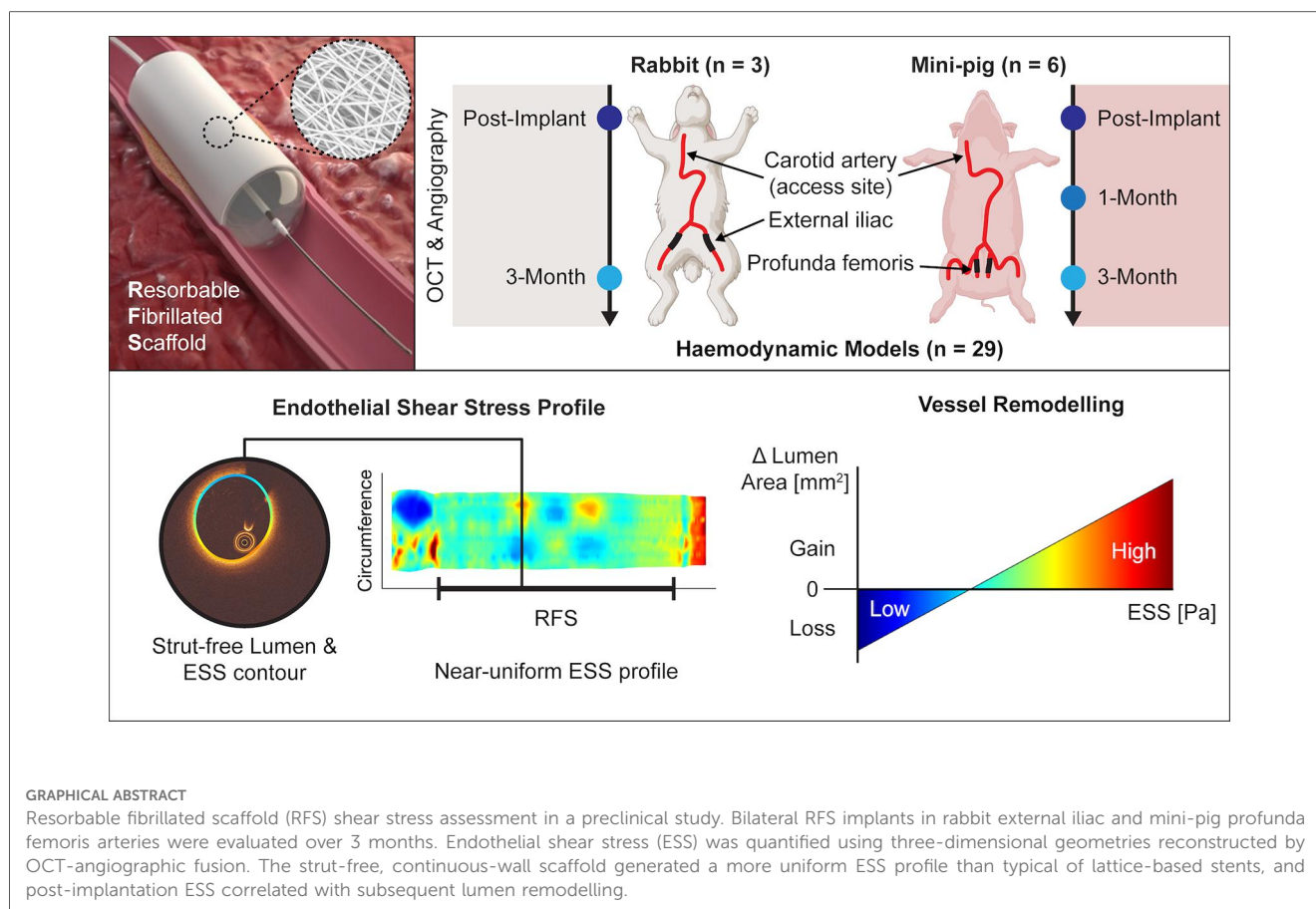
Methods: Three rabbits and six mini-pigs underwent bilateral implantation of a resorbable fibrillated scaffold (RFS) in peripheral arteries. Intravascular optical coherence tomography (OCT) combined with angiography enabled generation of 29 case-specific three-dimensional reconstructions during a 3-month study period. Pulsatile, non-Newtonian computational fluid dynamics (CFD) quantified the endothelial shear stress (ESS).

Results: OCT demonstrated a continuous endoluminal surface consistent with the strut-free RFS design and revealed a distinct optical transition at the device boundary. Haemodynamic mapping showed low-ESS regions at scaffold edges and broadly unidirectional near-wall flow within the scaffolded segment. Quantitatively, ESS showed a modest, non-significant upward trend during follow-up before stabilising (rabbits: +0.37 Pa, $p = 0.085$; mini-pigs: +0.37 Pa, $p = 0.091$). Higher early ESS correlated with subsequent lumen gain ($\rho_s = 0.50$; $p < 0.001$), and serial analyses revealed an evolving association over time.

Conclusion: RFS implantation instated a largely homogeneous ESS profile that evolved with 3-month remodelling, consistent with a dynamic flow-healing interplay that warrants longer-term evaluation through full bioresorption.

KEYWORDS

bioresorbable vascular scaffold, computational fluid dynamics, endothelial shear stress, optical coherence tomography, resorbable fibrillated scaffold



1 Introduction

Contemporary interventional cardiology relies heavily on drug-eluting stents (DES), which continue to deliver excellent revascularization outcomes across diverse lesions and patient profiles (1). Nevertheless, the permanent metallic lattice can impair vasomotion and mechanotransduction, delay endothelial healing, complicate re-intervention, and precipitate adverse events such as very late stent thrombosis (2). Bioresorbable vascular scaffolds (BVS) were developed to provide temporary support and restore natural vascular function after resorption. While first-generation BVS showed higher early thrombosis and target-lesion failure, these excess risks attenuate with longer follow-up and outcomes approach those of DES (3). Encouraging results in below-the-knee applications have renewed interest in a “cage-free” vessel (4) and driven next-generation designs.

The goal of “biorestorative” scaffolds is to resorb while fostering vascular healing (5). The Resorbable Fibrillated Scaffold (RFS) is one such device which combines a tubular, strut-free design with a porous, fibre-based polymer microarchitecture (STENTiT B.V., Eindhoven, the Netherlands). Preclinical data suggest that its fibrillated (acellular) matrix serves as a template for elastin-rich,

organised neotissue ingrowth, and promotes rapid re-endothelialisation (6). Elastin enrichment is noteworthy because it is a hallmark of healthy arterial structure and confers resistance to atherosclerosis (7).

Any intravascular scaffold, including biorestorative devices, alters lumen geometry and reshapes near-wall flow. These geometric changes modify local endothelial shear stress (ESS), a key mechanobiological determinant of endothelial phenotype and vascular health. High-resolution intravascular imaging combined with computational fluid dynamics (CFD) enables case-specific characterisation of microscopic, scaffold-induced flow disturbances, which have been linked to restenosis, thrombosis, and long-term device performance (8–14).

Despite promising preclinical healing features, the haemodynamic performance of the RFS has not been characterised. A first-in-human feasibility study (VITAL-IT 1) is evaluating its use in below-the-knee chronic limb-threatening ischaemia, highlighting the importance of mechanistic data. We therefore combined optical coherence tomography (OCT)-angiography fusion with CFD in two animal models to: (i) map ESS immediately after implantation, (ii) track its 3-month evolution during resorption, and (iii) identify early near-wall haemodynamic patterns that may inform subsequent vascular remodelling.

2 Methodology

All procedures were approved by the Utrecht University Institutional Ethical Committee and the Dutch Central Authority for Scientific Procedures on Animals (Rabbits: AVD2290020186144, 04 September 2018; Mini-pigs: AVD22900202216226, 05 June 2023) and conducted at the Gemeenschappelijk Dierenlaboratorium facility, Utrecht. The study complied with ARRIVE guidelines, EU Directive 2010/63, and NIH standards for animal research.

2.1 Experimental design

The RFS was fabricated by electrospinning (Vivolta, Waalre, the Netherlands) a poly-lactic-based co-polymer (Corbion Purac, Gorinchem, the Netherlands) into a strut-free tubular construct without anti-proliferative coating. The near-wall haemodynamic performance of the RFS was evaluated in two preclinical models (rabbits and mini-pigs). Both species are established platforms for evaluating the feasibility, safety and biocompatibility of vascular stents (15). As exploratory feasibility studies, group sizes were selected pragmatically rather than by sample size calculations. Blinding was not applied, as all animals received the same intervention and no untreated control group was included.

Three 12–15-week-old male New Zealand White rabbits (Charles River, France; body weight 2.4–2.8 kg) underwent bilateral implantation of 2.0 mm × 10 mm × 220 μm (inner diameter × length × nominal thickness) RFS's in the external iliac arteries via a carotid approach. Angiography and OCT imaging were performed immediately post-implantation and at 3-month follow-up.

The RFS was upscaled to 3.0 mm × 27 mm for implantation in a porcine model to mimic the dimensions of human below-the-knee intervention. Using carotid access, RFS's were implanted bilaterally in the profunda femoris arteries of six female 15–17-month-old Göttingen mini-pigs (Ellegaard, Dalmoose, Denmark; body weight 35.0–41.0 kg). Angiography and OCT were performed immediately post-implantation and again at 1- and 3-month follow-ups.

Additional details of animal care, anaesthesia, analgesia, and perioperative management are provided in the [Supplementary Methodology 1, 2](#), with the study design and imaging inclusion/exclusion workflow shown in [Supplementary Figure S1](#).

2.2 Image acquisition and analysis

Contrast angiography and intravascular OCT were performed immediately after scaffold implantation and at scheduled follow-up. Angiography was obtained with animals positioned supine in an anteroposterior view for standardized assessment of vessel patency and scaffold placement. Cine runs were recorded at 15 frames/s and exported in DICOM (1,024 × 1,024 pixels)

format. OCT imaging (St. Jude Medical, St. Paul, MN, USA) used an automatic pullback of 18 mm/s at 180 frames/s, following intracoronary contrast flushing to clear the imaging field.

Imaging data was analysed offline by an independent core laboratory (CORRIB Laboratory, University of Galway, Ireland). For each case, two anatomical segments were defined:

1. Region of interest (ROI): the vessel portion reconstructed into a three-dimensional model for haemodynamic analysis
2. Scaffolded Segment (RFS): the vessel length treated with the RFS, delimited by its proximal and distal edges.

Side-branch landmarks visible in both angiography and OCT were catalogued by their axial position and circumferential orientation. These fiducials enabled co-registration of the two modalities and ensured that serial analyses surveyed the same vessel segment at each follow-up. ROI boundaries were set at the nearest proximal and distal landmarks; if a landmark lay within 3 mm of a scaffold edge, the next closest landmark was selected instead. Under OCT, the side branch location was defined at the carina, corresponding to the frame immediately before confluence of the side-branch and main vessel.

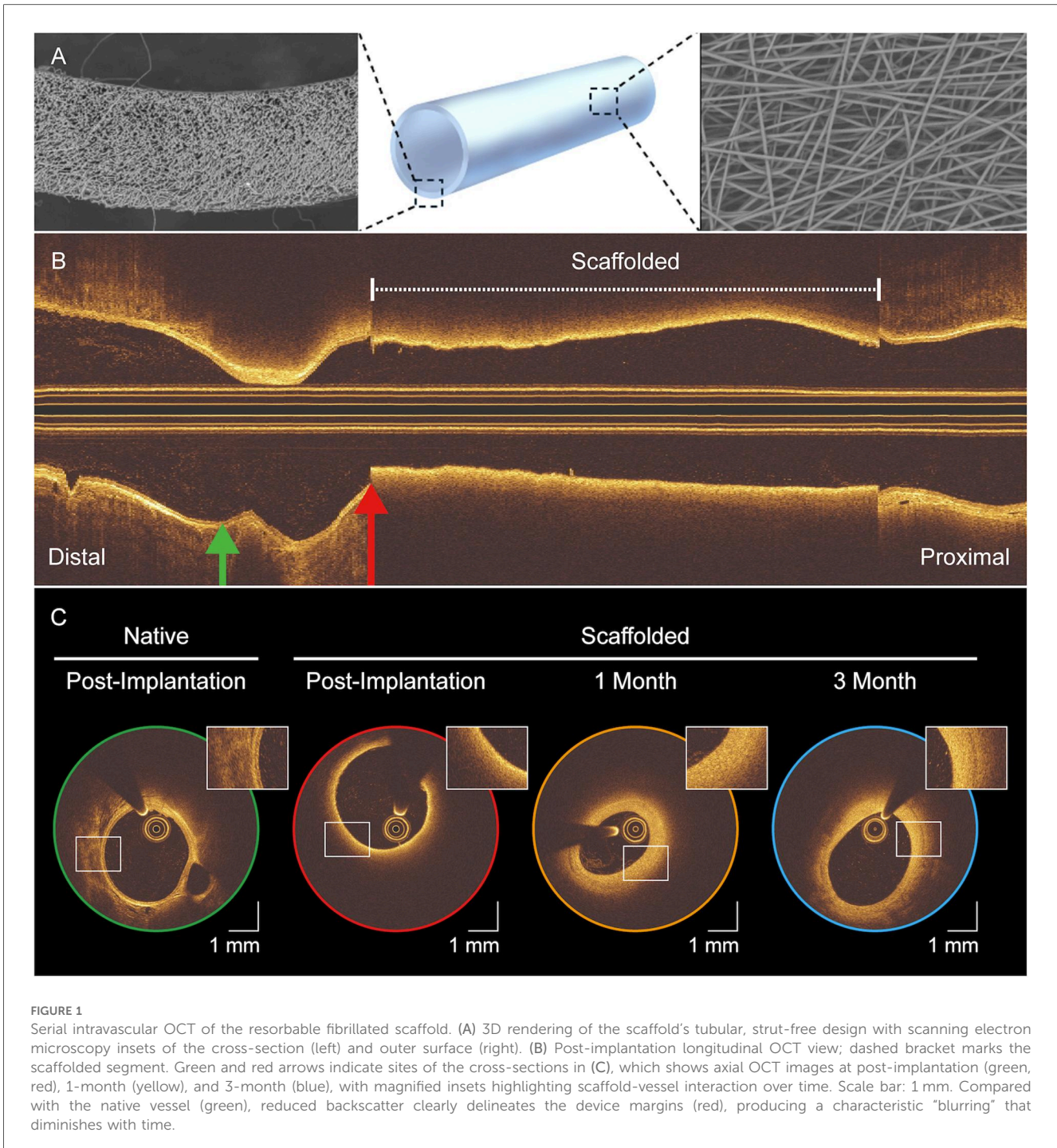
Unlike other bioresorbable scaffolds which incorporate metallic markers or radio-opaque composites (16), the RFS lacked such features, necessitating OCT for edge localization (see [Figure 1](#)). Nevertheless, the RFS exhibited a distinctive optical signature: its fibrillated architecture produces near-field optical scatter that shadows underlying anatomic structures, creating an abrupt transition. Scaffold edges were identified in the OCT frame where this optical scatter effect completely encircled the lumen (see [Supplementary Video S1](#)).

OCT pullbacks were analysed at 100 μm intervals along both the ROI and scaffold-treated (RFS) segments. Three metrics were calculated: (i) segment length (mm); (ii) minimum lumen area (MLA, mm²); and (iii) lumen volume (LV, mm³) (17).

2.3 Three-dimensional reconstruction

Three-dimensional reconstructions of the case-specific arterial geometry were performed by fusing the monoplane-derived angiographic centreline with OCT lumen cross-sections. Typically, in the coronary arteries two angiographic views separated by at least 25 degrees are preferred to ensure an accurate 3D centreline reconstruction. However, in this case, the vessel centreline was extracted from the only available single anteroposterior (AP) angiogram. As both external iliac and profunda femoris arteries lie predominantly in the coronal plane, the AP projection aligns this plane with the detector, minimizing foreshortening and rendering a monoplane acquisition sufficient for 3D reconstruction.

Vessel lumen contours were then semi-automatically extracted from OCT data within the ROI (QCU-CMS-v4.69, Leiden University Medical Centre, Leiden, the Netherlands). Finally, according to expert guidelines (18), these contours were precisely placed perpendicularly to the angiographic centreline using the catalogued anatomic landmarks to estimate their



absolute orientation (MATLAB R2024b, MathWorks Inc., Natick, MA, United States) (19). Unlike conventional strut-based stent designs, the RFS forms a closed, tubular conduit without lateral openings. As a result, blood flow can enter and exit the graft only at its proximal and distal margins, and the grafted segment was modelled as a single conduit consistent with its physical structure. The pipeline for co-registration and three-dimensional reconstruction is shown in [Supplementary Figure S2](#), and an overview of the final reconstructed vessel geometries is provided in [Supplementary Figure S3](#).

2.4 Haemodynamic assessment

Computational fluid dynamics (CFD) was employed to evaluate the haemodynamic environment of the RFS. For each reconstructed case, a computational mesh was generated for accurate haemodynamic modelling. This finite-volume mesh consisted of at least five layers of prism elements with the initial prism layer thickness set to 0.05 mm and a 10% increment with each subsequent layer. This layering strategy ensured adequate resolution near the lumen surface to accurately capture the

velocity gradient. To ensure spatial independence, mesh resolution was selected using physics-based near-wall criteria appropriate for laminar arterial flow, targeting $y^+ < 1$ based on the mean blood flow velocity and proximal (inlet) diameter (20). The resulting smallest mesh elements were then used to determine the temporal resolution from the local convective time scale, with time-step selection primarily constrained by flow pulsatility to ensure smooth representation of systolic acceleration and deceleration. Further details are provided in [Supplementary Methodology 3](#).

CFD modelling was performed using an in-house validated finite-volume method based on the robust open-source CFD toolbox (OpenFOAM v7, The OpenFOAM Foundation Ltd., London, UK). Appropriate boundary conditions were selected for each case, with mean inflow velocity estimated using the Thrombolysis in Myocardial Infarction (TIMI) frame count for the rabbit models (21). In mini-pigs, several angiograms were acquired only after full contrast opacification of the vessel, precluding reliable TIMI-based estimates; therefore, an empirically derived flow-diameter scaling law was applied in these cases (22). Given the lack of direct blood velocity measurements, a generic peripheral arterial waveform was prescribed at the inlet for both animal cohorts to represent physiological pulsatility, with the mean inflow magnitude scaled to match the aforementioned species-specific velocity estimates (23, 24). As blood viscosity was not measured directly, we adopted the standard Quemada constitutive model (25), consistent with prior studies showing that the animal and human blood share similar shear-thinning behaviour (26, 27). In the absence of electrocardiogram data, heart rates of 150 beats/minute (rabbits) (28), and 75 beats/minute (mini-pigs) (29) were assumed. Three cardiac cycles were simulated to dissipate initial transients. Relevant haemodynamic metrics were collected throughout the third cardiac cycle and were time-averaged. Key CFD set-up conditions are summarized in [Supplementary Table S1](#).

We evaluated several haemodynamic indices to characterise near-wall flow. The primary measure was endothelial shear stress (ESS) (see [Supplementary Video S2](#)). Additional indices included the ESS gradient (ESSG), transverse ESS (transESS), oscillatory shear stress (OSI), and the relative residence time (RRT), each capturing complementary aspects of shear stress magnitude, direction, and flow stagnation (see [Supplementary Table S2](#)). Results were projected onto a two-dimensional “carpet view” by virtually opening the vessel along its longitudinal direction and unrolling the luminal surface into a planar map spanning axial length and circumferential position. This post-processing representation enables continuous visualisation of near-wall haemodynamic patterns along the vessel at a uniform resolution ($0.1 \text{ mm} \times 1^\circ$).

2.5 Statistical analysis

Continuous variables were summarised as mean \pm SD when approximately normally distributed, or as median (IQR) when skewed. Categorical variables were expressed as counts (%). Temporal changes in OCT- and CFD-derived parameters were

analysed using linear mixed-effects models, which account for within-subject correlation and accommodate unbalanced longitudinal data. Time [post-implantation (PI), 1 month (1M), 3 months (3M)] was specified as a fixed effect, and Animal ID was included as a random intercept. When two or more time-point contrasts were available (e.g., in mini-pigs: PI, 1M, 3M), all pairwise comparisons were Bonferroni-adjusted. For rabbits (two time points: PI and 3M), only a single contrast was evaluated without adjustment. Model-estimated effects are reported as mean differences (Δ) with corresponding 95% confidence intervals (CI) and adjusted p -values. Associations between ESS and temporal change in lumen cross-sectional area (Δ CSA) were examined using Spearman’s rank correlation (ρ_s). A two-tailed $p < 0.05$ was considered statistically significant. All analyses were conducted in R (version 4.5.0; R Foundation for Statistical Computing, Vienna, Austria) using the *lme4*, *lmerTest*, and *emmeans* packages.

3 Results

3.1 Intravascular OCT imaging features

Twenty-nine OCT pullbacks were analysed (8 rabbits, 21 mini-pigs), comprising 15 504 frames. Key vessel metrics were evaluated using linear mixed-effects modelling, with model-derived temporal contrasts provided in [Supplementary Table S3](#) for full inferential detail. Case-specific scaffold lengths are illustrated in [Supplementary Figure S4](#).

In rabbits, scaffold length shortened by -1.55 mm [95% CI ($-1.87, -1.23$); $p < 0.001$] over 3 months, while changes in lumen volume and minimal lumen area within the scaffolded segment were not significant. In mini-pigs, marked early reductions occurred by 1 month: scaffold length -4.64 mm [95% CI ($-6.19, -3.10$); $p < 0.001$], MLA -3.27 mm^2 [95% CI ($-4.70, -1.84$); $p < 0.001$], and lumen volume -97.86 mm^3 [95% CI ($-130.50, -65.21$); $p < 0.001$]. Between 1 and 3 months, dimensions remained stable (all $p > 0.99$). Across the reconstructed vessel, similar trends were observed.

3.2 Qualitative assessment of shear stress post-implantation

Post-implantation, both species revealed characteristic shear stress patterns. Clearly defined regions of low ESS were observed at the scaffold edges ([Figures 2A,B](#)). Within the scaffold, ESS was broadly homogeneous; rabbit cases additionally exhibited a subtle criss-cross motif. Within the RFS-segment, multidirectional indices demonstrated predominately unidirectional near-wall flow patterns ([Supplementary Figure S5](#)).

3.3 Temporal changes in shear stress

ESS showed a non-significant upward tendency in both species (see [Figure 3](#)). In rabbits, ESS increased by $+0.37 \text{ Pa}$ [95% CI

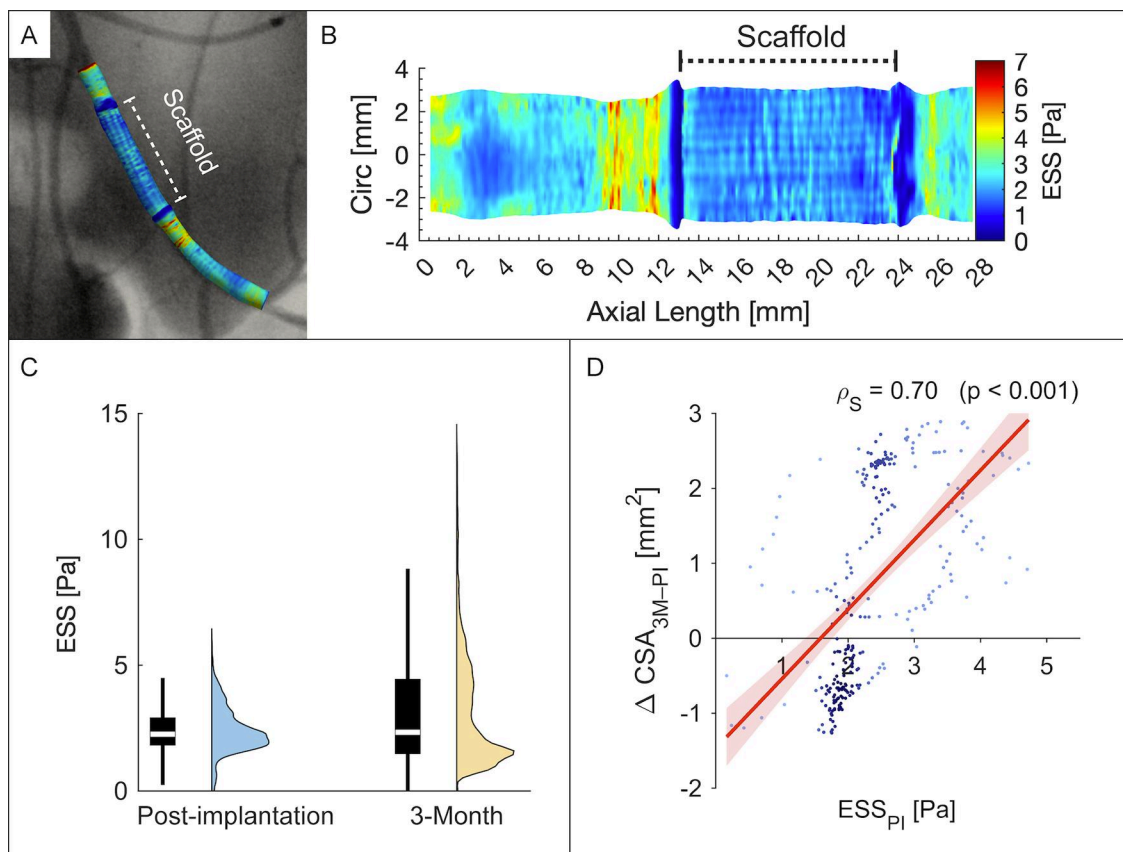


FIGURE 2

Endothelial shear stress in a representative rabbit external iliac artery. (A) Three-dimensional reconstruction of the left iliac artery showing post-implantation ESS co-registered with angiography. (B) Carpet plot of ESS distribution along vessel length and circumference; dashed bracket marks the scaffolded segment. (C) Violin/boxplots of ESS at post-implantation (blue) and 3 months (yellow). (D) Scatterplot of post-implantation ESS (ESS_{PI}) versus 3-month change in lumen cross-sectional area [$\Delta \text{CSA}_{3\text{M-PI}}$ (mm²)]; points coloured by density (dark to light blue). Circ, circumference.

($-0.09, 0.83$); $p = 0.085$, single contrast]. In mini-pigs, ESS rose by a similar $+0.37$ Pa at 1 month vs. baseline [95% CI ($-0.05, 0.80$); $p = 0.091$] and then plateaued through 3 months. Overall, changes did not reach statistical significance after adjustment, but both cohorts exhibited the same directional trend. Complementary indices (ESSG, transESS, OSI, RRT) exhibited comparable temporal fluctuations (see [Supplementary Figure S6](#)).

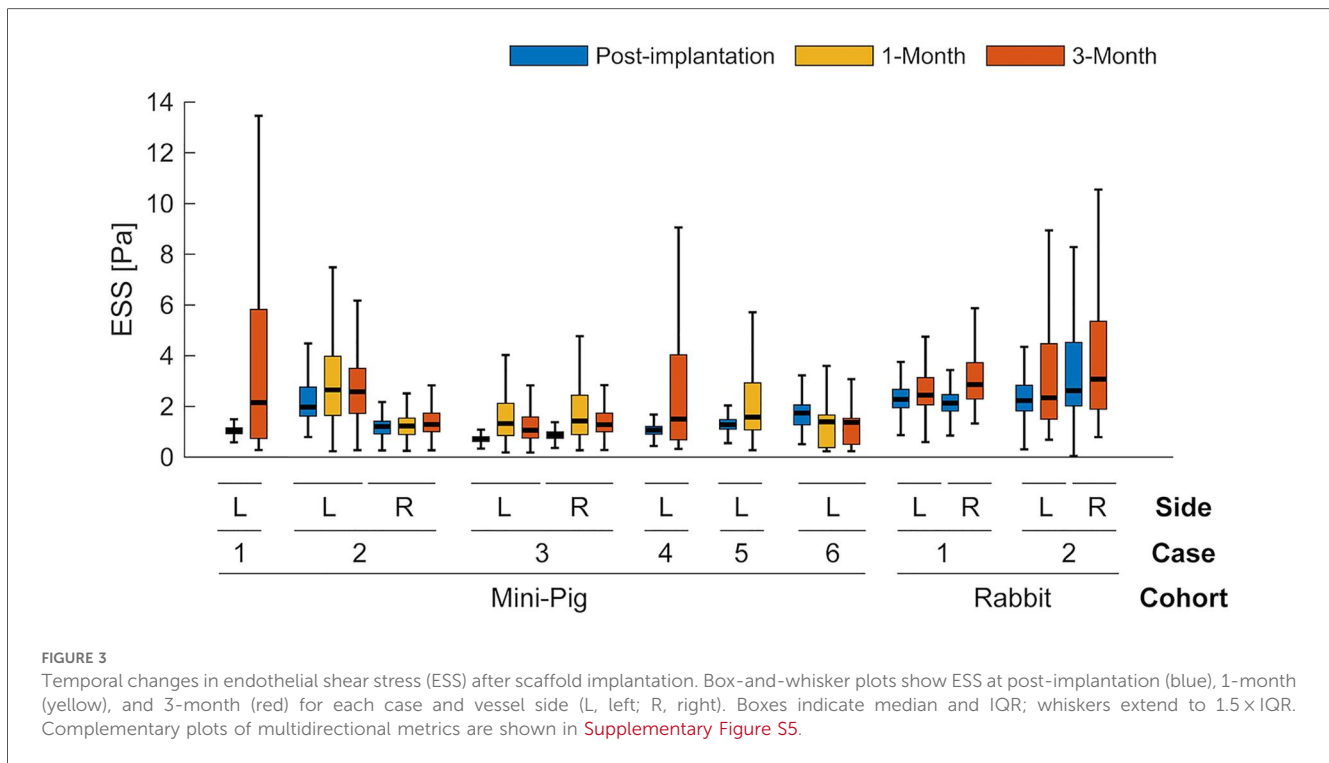
3.4 Shear stress and luminal remodelling

Figure 4 presents the association between ESS and ΔCSA at each time interval. In rabbits, a moderate positive correlation was observed between post-implantation ESS and ΔCSA at 3 months ($\rho_s = 0.50$, $p < 0.001$, $n = 4$; [Figure 4A](#)), with one vessel showing a notably stronger relationship ($\rho_s = 0.70$, $p < 0.001$; [Figure 2D](#)). In mini-pigs, post-implantation ESS correlated weakly with ΔCSA at 1 month ($\rho_s = 0.16$, $p < 0.001$, $n = 6$; [Figure 4B](#)). However, a strengthened correlation emerged between ESS at 1 month and ΔCSA at 3 months ($\rho_s = 0.36$, $p < 0.001$, $n = 5$; [Figure 4C](#)).

4 Discussion

In this study, the near-wall haemodynamic performance of the RFS was successfully evaluated for the first time in two preclinical models. The scaffolded segment displayed a distinctive shear profile at post-implantation, marked by minimal spatial variability in ESS (see [Figures 2A,B](#)). This homogeneity likely reflects the scaffold's strut-free design, supported by OCT findings that revealed a continuous endoluminal surface (see [Figure 1C](#)). However, rabbit haemodynamic maps exhibited a faint criss-cross ESS motif. In such cases, OCT revealed subtly polygonal, approximately decagonal luminal cross-sections rather than circular ones (see [Supplementary Video S1](#)), plausibly reflecting mild oversizing or nuances in balloon-scaffold mounting. The motif was discernible only with ultra-high-resolution OCT, underscoring its value for resolving fine, local flow phenomena (10, 12).

Protruding stent struts create microscopic obstacles for flowing blood. This irregular geometry generates flow separation, recirculation, and low and oscillatory shear niches, conditions linked to inflammation, thrombosis and neointimal



hyperplasia (30–35). ABSORB BVS shows an initial high–low ESS pattern across successive struts that homogenises by five years as the scaffold resorbs (9). In contrast, the RFS installs a smooth, strut-free endoluminal contour that mimics the native vessel (“vasculo-mimetic”). Consistent with this design, near-wall haemodynamics was predominantly unidirectional, lacking zones of low or oscillatory ESS (see [Supplementary Figure S5](#)).

We sought to determine whether this favourable haemodynamic environment translated into reduced neointimal formation. However, OCT-based evaluation was hindered by optical backscatter from the fibrillated scaffold microarchitecture, which obscured delineation of tissue-scaffold borders and prevented precise quantification (see [Figure 1C](#)). Consequently, although the ESS distributions suggests a favourable haemodynamic environment free of disturbed near-wall flow, which may mitigate maladaptive intimal thickening, direct confirmation requires histological validation and complementary imaging modalities (36). Nevertheless, the identification of this unique, device-specific optical artefact represents an important observation in OCT characterisation of the RFS.

ESS correlated with lumen area changes, with a stronger association in rabbits than in mini-pigs. This difference may partly reflect inflow boundary condition assumptions, using case-specific TIMI frame-counts in rabbits vs. a generalized flow-diameter scaling law in mini-pigs. Nevertheless, unlike conventional open- or closed-cell lattice stents that expose the wall to shear stress, the RFS’s continuous surface tubular design partially shields the vessel immediately post-implantation. However, rapid re-endothelialisation observed preclinically (37) likely reconstitutes the shear-sensing interface soon after. In

mini-pigs, ESS at the first follow-up correlated more strongly with subsequent lumen changes than post-implant ESS (see [Figure 4](#)). Although causality remains unproven, this shift may reflect evolving endothelial responsiveness to ESS and suggests that tissue integration into the fibrillated scaffold, as observed preclinically (6), could promote vascular restoration.

Current regulatory evaluations of stents, such as those by the FDA, focus largely on mechanical performance and do not account for haemodynamic behaviour. Future scaffold designs should incorporate CFD-informed assessments (38). At the proximal and distal scaffold edges, OCT revealed distinct “step-up” and “step-down” transitions, respectively. These abrupt shifts between scaffolded and native vessel segments induced recirculating, low-velocity flow, forming low-shear stress rings. Such edge effects are clinically relevant, as they can promote restenosis and thrombosis (30, 39). Despite its strut-free profile, edge geometry remained a key determinant of local flow. Owing to modest scaffold shortening, assessment of shear-induced remodelling at device edges was limited. Nevertheless, lumen loss at follow-up consistently localised to edge regions that had been exposed to low ESS at implantation (see [Supplementary Figure S5](#)). Building on prior findings (13, 38, 40), thin, tapered, or curved edge transitions can reduce flow separation, increase local ESS, and minimize recirculation. However, these haemodynamic benefits must be balanced against the reduced mechanical strength of polymer-based materials compared to metals, as thinner walls risk radial collapse. Tapered edges provide validated haemodynamic advantages but must meet structural requirements for acute support and long-term safety. Balancing mechanical stability with optimal shear characteristics is critical for promoting vascular healing.

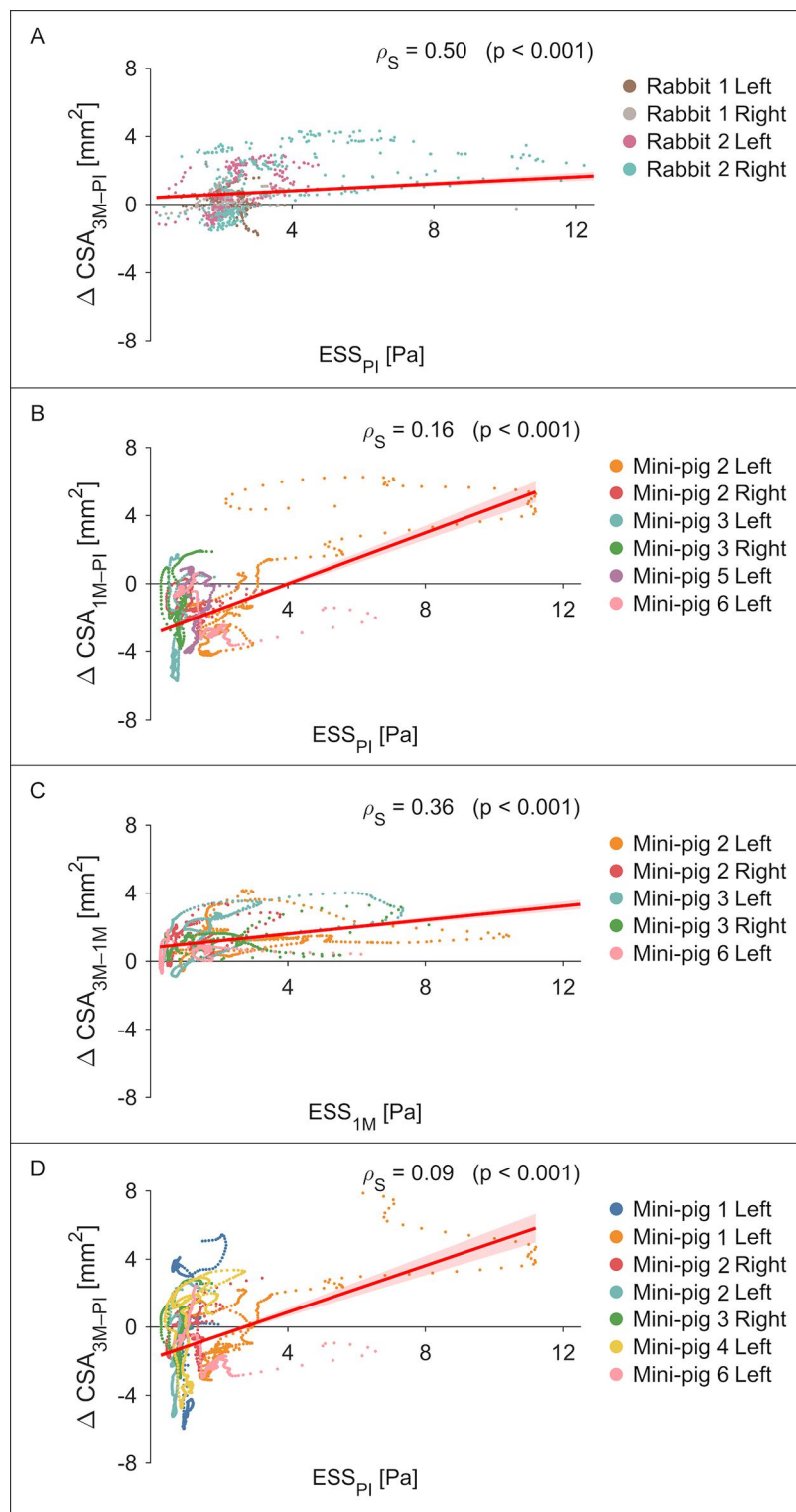


FIGURE 4

Endothelial shear stress and subsequent changes in lumen cross-sectional area. Scatterplots are shown for each case (unique colours): rabbits at (A) post-implantation vs. 3-month, and mini-pigs at (B) post-implantation vs. 1-month, (C) 1-month vs. 3-month, and (D) post-implantation vs. 3-month. For each cross-section, ESS was averaged over the full circumference. Spearman's rank correlation (ρ_s) and p -value are reported in each panel. Linear regression lines with 95% confidence intervals (red shading) illustrate the trend.

This preliminary animal study has several limitations. This preliminary animal study has several limitations. First, the sample size was modest, and findings should be considered exploratory. However, each animal underwent bilateral implantation with serial follow-up, yielding repeated haemodynamic and morphological measurements per subject, providing a rich dataset appropriate for early-stage feasibility and hypothesis-generating analyses. Second, imaging was monoplane rather than biplane; however, vessels anatomy was largely planar, limiting foreshortening. Finally, rabbit inflows estimates were case-specific (TIMI), whereas mini-pig simulations relied on scaled estimates.

RFS implantation instated a broadly homogeneous ESS profile, consistent with its strut-free, continuous-wall design. This pattern evolved with vessel remodelling, underscoring the dynamic interplay between shear stress and vascular healing. These preliminary findings warrant longer-term evaluation to elucidate scaffold-flow interactions throughout full bioresorption and to enable comparison with lattice-based stents.

Data availability statement

The original contributions presented in the study are included in the article/[supplementary material](#), further inquiries can be directed to the corresponding authors.

Ethics statement

The animal study was approved by Utrecht University Institutional Ethical Committee and the Dutch Central Authority for Scientific Procedures on Animals (Rabbits: AVD2290020186144, 04 September 2018; Mini-pigs: AVD22900202216226, 05 June 2023). The study was conducted in accordance with the local legislation and institutional requirements.

Author contributions

LH: Data curation, Formal analysis, Visualization, Writing – original draft, Writing – review & editing. KM: Data curation, Writing – review & editing. RdV: Investigation, Writing – review & editing. BS: Resources, Writing – review & editing. GvB: Resources, Writing – review & editing. KvN: Investigation, Writing – review & editing. JD: Methodology, Software, Writing – review & editing. CB: Writing – review & editing. TT: Writing – review & editing. YO: Conceptualization, Supervision, Writing – review & editing. PB: Conceptualization, Supervision, Writing – review & editing. PS: Conceptualization, Supervision, Writing – review & editing. EP: Conceptualization, Formal analysis, Software, Supervision, Writing – review & editing.

Funding

The author(s) declared that financial support was received for this work and/or its publication. BS, GvB, RdV, and KvN declared that financial support was received for this work and/or its publication [Smart Biomaterials Consortium (STE-22-01)]. All other authors did not receive funding for this study.

Acknowledgments

The computational analysis was supported by the Research Computing Services NCI (National Computational Infrastructure) Access scheme at The University of Melbourne.

Conflict of interest

GvB and BS are shareholders of STENTiT B.V.; RdV is employed by STENTiT B.V. as a preclinical engineer, and KvN oversees its clinical affairs.

The remaining author(s) declared that this work was conducted in the absence of any commercial or financial relationships that could be construed as a potential conflict of interest.

The author CB declared that they were an editorial board member of *Frontiers*, at the time of submission. This had no impact on the peer review process and the final decision.

Generative AI statement

The author(s) declared that generative AI was not used in the creation of this manuscript.

Any alternative text (alt text) provided alongside figures in this article has been generated by *Frontiers* with the support of artificial intelligence and reasonable efforts have been made to ensure accuracy, including review by the authors wherever possible. If you identify any issues, please contact us.

Publisher's note

All claims expressed in this article are solely those of the authors and do not necessarily represent those of their affiliated organizations, or those of the publisher, the editors and the reviewers. Any product that may be evaluated in this article, or claim that may be made by its manufacturer, is not guaranteed or endorsed by the publisher.

Supplementary material

The Supplementary Material for this article can be found online at: <https://www.frontiersin.org/articles/10.3389/fcvm.2026.1744904/full#supplementary-material>

References

- Palmerini T, Benedetto U, Biondi-Zoccai G, Della Riva D, Bacchi-Reggiani L, Smits PC, et al. Long-term safety of drug-eluting and bare-metal stents: evidence from a comprehensive network meta-analysis. *J Am Coll Cardiol.* (2015) 65(23):2496–507. doi: 10.1016/j.jacc.2015.04.017
- Madhavan MV, Kirtane AJ, Redfors B, Généreux P, Ben-Yehuda O, Palmerini T, et al. Stent-related adverse events >1 year after percutaneous coronary intervention. *J Am Coll Cardiol.* (2020) 75(6):590–604. doi: 10.1016/j.jacc.2019.11.058
- Power DA, Camaj A, Kereiakes DJ, Ellis SG, Gao R, Kimura T, et al. Early and late outcomes with the absorb bioresorbable vascular scaffold. Final report from the ABSORB clinical trial program. *JACC Cardiovasc Interv.* (2025) 18(1):1–11. doi: 10.1016/j.jcin.2024.08.050
- Varcoe RL, DeRubertis BG, Kolluri R, Krishnan P, Metzger DC, Bonaca MP, et al. Drug-eluting resorbable scaffold versus angioplasty for infrapopliteal artery disease. *N Engl J Med.* (2024) 390(1):9–19. doi: 10.1056/NEJMoa2305637
- Ono M, Kageyama S, O'Leary N, El-Kurdi MS, Reinöhl J, Solien E, et al. 1-year patency of bioresorbative polymeric coronary artery bypass grafts in an ovine model. *JACC Basic Transl Sci.* (2023) 8(1):19–34. doi: 10.1016/j.jacpts.2022.06.021
- Duijvelshoff R, Cabrera Maria S, Sanders B, Dekker S, Smits Anthal IPM, Baaijens Frank PT, et al. Transcatheter-delivered expandable bioresorbable polymeric graft with stenting capacity induces vascular regeneration. *JACC Basic Transl Sci.* (2020) 5(11):1095–110. doi: 10.1016/j.jacpts.2020.09.005
- Otsuka F, Yahagi K, Sakakura K, Virmani R. Why is the mammary artery so special and what protects it from atherosclerosis?. *Ann Cardiothorac Surg.* (2013) 2(4):519–26. doi: 10.3978/j.issn.2225-319X.2013.07.06
- Bourantas CV, Papafaklis MI, Lakkas L, Sakellarios A, Onuma Y, Zhang YJ, et al. Fusion of optical coherence tomographic and angiographic data for more accurate evaluation of the endothelial shear stress patterns and neointimal distribution after bioresorbable scaffold implantation: comparison with intravascular ultrasound-derived reconstructions. *Int J Cardiovasc Imaging.* (2014) 30(3):485–94. doi: 10.1007/s10554-014-0374-3
- Thondapu V, Tenekecioglu E, Poon EKW, Collet C, Torii R, Bourantas CV, et al. Endothelial shear stress 5 years after implantation of a coronary bioresorbable scaffold. *Eur Heart J.* (2018) 39(18):1602–9. doi: 10.1093/eurheartj/ehx810
- Poon EKW, Wu X, Dijkstra J, O'Leary N, Torii R, Reiber JHC, et al. Angiography and optical coherence tomography derived shear stress: are they equivalent in my opinion?. *Int J Cardiovasc Imaging.* (2023) 39(10):1953–61. doi: 10.1007/s10554-023-02949-0
- Poon EKW, Ono M, Wu X, Dijkstra J, Sato Y, Kutyna M, et al. An optical coherence tomography and endothelial shear stress study of a novel bioresorbable bypass graft. *Sci Rep.* (2023) 13(1):2941. doi: 10.1038/s41598-023-29573-1
- Poon EKW, Ninomiya K, Kageyama S, Guo X, Reimers B, Torii R, et al. Two facets of shear stress post drug coating balloon: angiography versus optical coherence tomography fusion approach. *Circ Cardiovasc Imaging.* (2024) 17(4):e016279. doi: 10.1161/CIRCIMAGING.123.016279
- Tenekecioglu E, Torii R, Bourantas CV, Sotomi Y, Cavalcante R, Zeng Y, et al. Difference in haemodynamic microenvironment in vessels scaffolded with absorb BVS and mirage BRMS: insights from a preclinical endothelial shear stress study. *EuroIntervention.* (2017) 13(11):1327–35. doi: 10.4244/EIJ-D-17-00283
- Tenekecioglu E, Torii R, Katagiri Y, Chichareon P, Asano T, Miyazaki Y, et al. Post-implantation shear stress assessment: an emerging tool for differentiation of bioresorbable scaffolds. *Int J Cardiovasc Imaging.* (2019) 35(3):409–18. doi: 10.1007/s10554-018-1481-3
- Schwartz RS, Edelman E, Virmani R, Carter A, Granada JF, Kaluza GL, et al. Drug-eluting stents in preclinical studies. *Circ Cardiovasc Interv.* (2008) 1(2):143–53. doi: 10.1161/CIRCINTERVENTIONS.108.789974
- Shen Y, Tang C, Sun B, Wu Y, Yu X, Cui J, et al. Development of 3D printed biodegradable, entirely x-ray visible stents for rabbit carotid artery implantation. *Adv Healthcare Mater.* (2024) 13(15):2304293. doi: 10.1002/adhm.202304293
- Araki M, Park S-J, Dauerman HL, Uemura S, Kim J-S, Di Mario C, et al. Optical coherence tomography in coronary atherosclerosis assessment and intervention. *Nat Rev Cardiol.* (2022) 19(10):684–703. doi: 10.1038/s41569-022-00687-9
- Gijsen F, Katagiri Y, Barlis P, Bourantas C, Collet C, Coskun U, et al. Expert recommendations on the assessment of wall shear stress in human coronary arteries: existing methodologies, technical considerations, and clinical applications. *Eur Heart J.* (2019) 40(41):3421–33. doi: 10.1093/eurheartj/ehz551
- Athanasios LS, Bourantas CV, Siogkas PK, Sakellarios AI, Exarchos TP, Naka KK, et al. 2012 annual international conference of the IEEE engineering in medicine and biology society. *3D Reconstruction of Coronary Arteries Using Frequency Domain Optical Coherence Tomography Images and Biplane Angiography*; IEEE (2012).
- Inthavong K, Chetty A, Shang Y, Tu J. Examining mesh independence for flow dynamics in the human nasal cavity. *Comput Biol Med.* (2018) 102:40–50. doi: 10.1016/j.compbiomed.2018.09.010
- Coskun AU, Yeghiazarians Y, Kinlay S, Clark ME, Ilegbusi OJ, Wahle A, et al. Reproducibility of coronary lumen, plaque, and vessel wall reconstruction and of endothelial shear stress measurements *in vivo* in humans. *Catheter Cardiovasc Interv.* (2003) 60(1):67–78. doi: 10.1002/ccd.10594
- van der Giessen AG, Groen HC, Doriot PA, de Feyter PJ, van der Steen AFW, van de Vosse FN, et al. The influence of boundary conditions on wall shear stress distribution in patients specific coronary trees. *J Biomech.* (2011) 44(6):1089–95. doi: 10.1016/j.jbiomech.2011.01.036
- Alastruey J, Nagel SR, Nier BA, Hunt AA, Weinberg PD, Peiró J. Modelling pulse wave propagation in the rabbit systemic circulation to assess the effects of altered nitric oxide synthesis. *J Biomech.* (2009) 42(13):2116–23. doi: 10.1016/j.jbiomech.2009.05.028
- Avolio AP, O'Rourke MF, Mang K, Bason PT, Gow BS. A comparative study of pulsatile arterial hemodynamics in rabbits and guinea pigs. *Am J Physiol.* (1976) 230(4):868–75. doi: 10.1152/ajplegacy.1976.230.4.868
- Poon EKW, Thondapu V, Hayat U, Barlis P, Yap CY, Kuo PH, et al. Elevated blood viscosity and microcirculation resulting from coronary stent malapposition. *J Biomech Eng.* (2018) 140(5). doi: 10.1115/1.4039306
- Caron A, Menu P, Faivre-Fiorina B, Labrude P, Alayash AI, Vigneron C. Cardiovascular and hemorheological effects of three modified human hemoglobin solutions in hemodiluted rabbits. *J Appl Physiol.* (1999) 86(2):541–8. doi: 10.1152/jappl.1999.86.2.541
- Horner J, Wagner N, Beris A. A comparative study of blood rheology across species. *Soft Matter.* (2021) 17:4766–74. doi: 10.1039/D1SM00258A
- Cubík J, Kepak S, Wiedermannova H, Vrtkova A, Burckova H, Zarubova P, et al. Measuring respiratory and heart rate using a fiber optic interferometer: a pilot study in a neonate model. *Front Pediatr.* (2022) 10:957835. doi: 10.3389/fped.2022.957835
- Kieslichová E, Zazula R, Skibová J, Ryska M, Pantoflíček T, Ryska O. Hemodynamic parameters in a surgical desvascularization model of fulminant hepatic failure in the minipig. *Physiol Res.* (2005) 54(5):485–90. doi: 10.33549/physiolres.930619
- Ng J, Bourantas CV, Torii R, Ang HY, Tenekecioglu E, Serruys PW, et al. Local hemodynamic forces after stenting. *Arterioscler Thromb Vasc Biol.* (2017) 37(12):2231–42. doi: 10.1161/ATVBAHA.117.309728
- Tenekecioglu E, Poon EKW, Collet C, Thondapu V, Torii R, Bourantas CV, et al. The nidus for possible thrombus formation: insight from the microenvironment of bioresorbable vascular scaffold. *JACC Cardiovasc Interv.* (2016) 9(20):2167–8. doi: 10.1016/j.jcin.2016.08.019
- Kolandaivelu K, Swaminathan R, Gibson WJ, Kolachalama VB, Nguyen-Ehrenreich K-L, Giddings VL, et al. Stent thrombogenicity early in high-risk interventional settings is driven by stent design and deployment and protected by polymer-drug coatings. *Circulation.* (2011) 123(13):1400–9. doi: 10.1161/CIRCULATIONAHA.110.003210
- Bourantas CV, Papafaklis MI, Kotsia A, Farooq V, Muramatsu T, Gomez-Lara J, et al. Effect of the endothelial shear stress patterns on neointimal proliferation following drug-eluting bioresorbable vascular scaffold implantation: an optical coherence tomography study. *JACC Cardiovasc Interv.* (2014) 7(3):315–24. doi: 10.1016/j.jcin.2013.05.034
- Wentzel JJ, Krams R, Schuurbijs JCH, Oomen JA, Kloet J, van der Giessen WJ, et al. Relationship between neointimal thickness and shear stress after wallstent implantation in human coronary arteries. *Circulation.* (2001) 103(13):1740–5. doi: 10.1161/01.CIR.103.13.1740
- Ahmed Mona E, Leistner David M, Hakim D, Abdelwahed Y, Coskun Ahmet U, Maynard C, et al. Endothelial shear stress metrics associate with proinflammatory pathways at the culprit site of coronary erosion. *JACC Basic Transl Sci.* (2024) 9(11):1269–83. doi: 10.1016/j.jacpts.2024.07.008
- Carlier SG, van Damme LCA, Blommerde CP, Wentzel JJ, van Langheve G, Verheye S, et al. Augmentation of wall shear stress inhibits neointimal hyperplasia after stent implantation. *Circulation.* (2003) 107(21):2741–6. doi: 10.1161/01.CIR.0000066914.95878.6D
- Hsiao ST, Spencer T, Boldock L, Prosseda SD, Xanthos I, Tovar-Lopez FJ, et al. Endothelial repair in stented arteries is accelerated by inhibition of Rho-associated protein kinase. *Cardiovasc Res.* (2016) 112(3):689–701. doi: 10.1093/cvr/cvw210
- Jiménez JM, Davies PF. Hemodynamically driven stent strut design. *Ann Biomed Eng.* (2009) 37(8):1483–94. doi: 10.1007/s10439-009-9719-9
- Koskinas KC, Chatzizisis YS, Antoniadis AP, Giannoglou GD. Role of endothelial shear stress in stent restenosis and thrombosis: pathophysiological mechanisms and implications for clinical translation. *J Am Coll Cardiol.* (2012) 59(15):1337–49. doi: 10.1016/j.jacc.2011.10.903
- Tarrahi I, Colombo M, Hartman EMJ, Tovar Forero MN, Torii R, Chiastra C, et al. Impact of bioresorbable scaffold design characteristics on local haemodynamic forces: an *ex vivo* assessment with computational fluid dynamics simulations. *EuroIntervention.* (2020) 16(11):e930–7. doi: 10.4244/EIJ-D-19-00657